

Article

Thermographic Stall Detection by Model-Inspired Evaluation of the Dynamic Temperature Behaviour

Felix Oehme ^{1,*} , Janick Suhr ² , Nicholas Balaesque ², Daniel Gleichauf ¹ , Michael Sorg ¹ 
and Andreas Fischer ¹ 

¹ Bremen Institute for Metrology, Automation and Quality Science, University of Bremen, Linzer Str. 13, 28359 Bremen, Germany; d.gleichauf@bimaq.de (D.G.); m.sorg@bimaq.de (M.S.); andreas.fischer@bimaq.de (A.F.)

² Deutsche WindGuard Engineering GmbH, Überseering 7, 27580 Bremerhaven, Germany; Janick.Suhr@windguard.de (J.S.); N.Balaesque@windguard.de (N.B.)

* Correspondence: f.oehme@bimaq.de

Abstract: Model-inspired signal processing approaches with an enhanced detectability of flow separation on thermographic images are presented. Flow separation causes performance loss, structural loads and increasing acoustic emissions on wind turbine rotor blades. However, due to the low thermal contrast between turbulent and separated flow regions, the non-invasive thermographic visualisation of flow separation is currently only possible for wind tunnel measurements, which are characterised by a high thermal contrast and a small measuring distance. The state-of-the-art signal processing approaches evaluate the surface temperature fluctuation of thermographic image series. However, understanding of the signal measurement chain with a distinct consideration of the influences on the dynamic surface temperature is incomplete. Therefore, designing model-inspired signal processing approaches which provide a high interpretability and a maximum contrast is an open task. The proposed signal processing approaches evaluate the surface response selectively, by using the amplitude information of the surface temperature response to an oscillating input signal or gradient-based for a transient input signal. The approaches are applied to wind tunnel measurements on a rotor blade profile at a near thermodynamic steady state and a transient thermodynamic behaviour at Reynolds numbers that are representative for operational wind turbines. The gradient-based evaluation shows an improved contrast for the detection of flow separation, but is only applicable to profiles with transient thermodynamic behaviour. The amplitude evaluation provides a high degree of interpretability of the processed images based on flow-dependent features and enables for an unambiguous identification of flow separation by a global amplitude minimum close to the separation point. Additionally, an increased spatial resolution for surface modifications is shown, while the contrast between flow regions is significantly decreased. Hence, the proposed approaches allow for an improved identifiability of flow separation with regard to future applications on wind turbines in operation.

Keywords: IR thermography; thermographic flow visualisation; thermographic boundary layer measurements; turbulent flow separation; flow separation



Citation: Oehme, F.; Suhr, J.; Balaesque, N.; Gleichauf, D.; Sorg, M.; Fischer, A. Thermographic Stall Detection by Model-Inspired Evaluation of the Dynamic Temperature Behaviour. *Appl. Sci.* **2021**, *11*, 8442. <https://doi.org/10.3390/app11188442>

Academic Editors: Sergio Montelpare, Renato Ricci and Valerio D'Alessandro

Received: 23 July 2021

Accepted: 9 September 2021

Published: 11 September 2021

Publisher's Note: MDPI stays neutral with regard to jurisdictional claims in published maps and institutional affiliations.



Copyright: © 2021 by the authors. Licensee MDPI, Basel, Switzerland. This article is an open access article distributed under the terms and conditions of the Creative Commons Attribution (CC BY) license (<https://creativecommons.org/licenses/by/4.0/>).

1. Introduction

For wind turbines with pitch control, turbulent flow separation is an undesirable phenomenon [1]. It induces a sudden decrease in torque-producing lift and an increase in drag [2,3]. Additionally, aerodynamic performance loss, structural loads and increasing acoustic emissions occur. Structural loads result from vibrations and can cause a reduced plant operating lifetime [4]. Acoustic emissions lead to a decrease in social acceptance of wind energy turbines and complicate the siting. To be able to investigate the origin of these effects as close as possible to a real wind turbine in operation, a contactless, non-invasive

imaging measurement method with in-process capability is required for the detection and localisation of flow separation on wind turbine rotor blades.

Long-established methods to detect and localise flow separation are tufts [5], stall flags [6], or oil solutions [7]. These methods are suitable for in-process measurements and are technologically easy to apply. However, the installation and precise positioning are time-consuming and costly. The techniques are also invasive, influence the boundary layer flow, and suffer from a poor spatial resolution along the rotor blade [8]. Thus, the available methods do not meet the requirements of a non-invasive, contactless, and imaging measurement system.

A measurement method with the potential to meet all requirements for measuring flow separation on wind turbines, even in process, is infrared (IR) thermographic flow visualisation [9]. The measuring principle of thermographic flow visualisation is based on the relation between the convective heat flux density and the boundary layer flow region. Under the condition of the presence of convective heat flow, i.e., a temperature difference between the incoming flow and the blade, different convective heat flux densities cause different surface temperatures on the rotor blade. The surface temperature differences are non-invasively measurable by detecting the IR radiation with a respective camera [10]. As a result, the visualisation of different boundary layer flow regions on the rotor blade is possible with a high image resolution.

In wind tunnel experiments, the measurement objects are usually actively, externally or internally, heated or cooled, to increase the necessary heat flux between the fluid and the rotor blade and, thus, to maximise the contrast of the thermographic images [8,11]. Since limiting measurement conditions exist for free-field measurements on distant wind turbines, active heating of the rotor blade is here excluded. The naturally available thermal difference between the rotor blade and the incoming flow exist solely due to solar radiation, which can be estimated to 175 W m^{-2} during summer on a cloud-free day [8]. Hence, the resulting low thermal contrast, together with the large distance between the rotor blade of a wind turbine and the thermographic camera on the ground, leads to the requirement of a thermographic measuring approach with enhanced sensitivity.

The thermographic detection and characterisation of the laminar-turbulent transition in wind tunnel tests is a well known technique for wind tunnel experiments [12–15]. A distinct difference in convective heat transfer exists between the laminar and turbulent flow, so that an evaluation of steady state temperature fields enables a distinction of the different flow regions [16,17]. This measurement approach in a *thermodynamic steady state* was successfully transferred to free-field measurements. First, Dollinger et al. localized the laminar-turbulent transition on wind turbines in operation to quantify flow disturbances caused by the contamination or erosion of the leading edge [18]. They also investigated the effects on the measurement uncertainty for the distinction of different boundary layer flow regions [19]. Furthermore, Gleichauf et al. [20] proposed to evaluate the time series of thermographic images using the non-negative matrix factorisation in order to increase the ability to distinguish between different boundary layer flow regions by reducing temperature gradients inside each flow region. Another approach for the thermographic localisation of the laminar-turbulent transition is to consider the *transient thermodynamic behaviour* on the rotor blade surface. Possible measurement setups to distinguish flow regions by heating rate are pitching rotor blades where the location of the different boundary layer flow regions changes [11,21] or non-pitching rotor blades with transient internal or external heating intensities [22]. Both measurement setups can increase the thermal contrast between different boundary layer flow regions and enable the investigation of the transient behaviour of the laminar-turbulent transition [11,22]. A transfer to wind turbines in operation with pitching airfoils or transient absorbed solar radiation seems feasible, but a study of the transient thermodynamic behaviour for localisation in particular separated flow regions is pending.

In contrast to the laminar-turbulent transition, a thermographic distinction between the turbulent boundary layer and the turbulent-separated flow, as well as the interpretation of

the turbulent-separated flow signature on IR thermograms, is still a challenging subject for wind tunnel experiments [12]. The heat transport mechanisms of the turbulent boundary layer and the turbulent-separated boundary layer flow are different [23] but have the same order of magnitude in the region of beginning separation [17]. Thus the thermal contrast, in the case of flow separation, is significantly lower compared to laminar-turbulent transitions.

First, Gartenberg and Roberts [12] detected stall on an airfoil with internal heating by evaluating temperature fields on single frames. Gardner et al. [24] reported a statistical approach for stall detection on an intensively heated airfoil. They proposed creating stall maps for helicopter rotor blades by evaluating an increase in the spatial temperature variation. Dollinger et al. [8] published an alternative thermography measurement method for stall detection on non-heated static airfoils, i.e., for low thermal contrast conditions. By evaluating the dynamic behaviour of the surface temperature by means of a standard deviation or Fourier amplitudes of the temperature time series, an increase in the distinguishability of the boundary layer flow regions was shown. Note that the common aim of both recent approaches is to identify characteristics in the behaviour of the spatiotemporal surface temperature. However, the understanding of the signal measurement chain is incomplete, since a distinct consideration of the different influences of the boundary layer flow characteristics (*desired sensitivity*) and the incoming flow temperature fluctuation as influencing quantity (*cross-sensitivity*) is missing. Additionally, a separate evaluation of the harmonic and transient components of the surface temperature is not conducted. For this reason, the question of how to design a signal processing schema that is robust and effectively visualises regions of flow separation cannot be answered. As a result, the thermographic stall visualisation by evaluating the dynamic behaviour of the thermodynamic fluid–structure interaction seems promising, but designing a signal-processing scheme that provides a high degree of interpretability and maximum contrast is an open task.

For this reason, the aim of the article is at first to model the rotor blade surface temperature response with respect to boundary layer flow characteristics *and* temporal temperature fluctuations of the external flow using system theory. Finally, two measurement principles for different measurement conditions are derived on the basis of the system modelling to provide thermographic stall visualisation with enhanced interpretability and contrast. In particular, a harmonic analysis of temporal temperature fluctuations around predefined operating points is investigated, considering the amplitude information. In addition, a temporal gradient-based evaluation of the transient thermodynamic blade behaviour is studied.

First, the measurement chain of thermographic flow visualisation is analysed, and the measurement principles based on the dynamic response of the surface temperature around an operating point (small-signal behaviour) and for a transient input signal (large-signal behaviour), respectively, are derived in Section 2. The experimental setup for the wind tunnel experiments with measurements for different flow velocities on a wind turbine airfoil is presented in Section 3. Note that the chosen flow conditions are similar to the conditions of in-process wind turbines. The experimental results regarding interpretability and distinguishability of the different flow regions are presented for both dynamic thermographic flow visualisation principles in Section 4. In particular, the achievable enhancement of image interpretability and contrast for stall detection is discussed. The article closes with a summary and outlook in Section 5.

2. Principle of Measurement

In case of temperature differences between the rotor blade surface of wind turbines and the incoming fluid, the thermographic measurable surface temperature correlates with the fluid–surface interaction in the boundary layer flow. However, the detected surface temperature is also influenced by other quantities. In order to derive novel measurement concepts with enhanced interpretability and contrast, the current understanding of the classical measurement chain of thermographic flow visualisation, including all influencing quantities is first presented.

For a differential volume element on the surface of a rotor blade—see Figure 1—the temperature T_s can be calculated using a heat balance, as follows

$$\rho \cdot c_P \cdot \frac{\partial T_s}{\partial t} = -\nabla \cdot \dot{q}. \tag{1}$$

As a result, spatial differences of the temperature on airfoils are influenced by spatial changes in density ρ and specific heat capacity c_P , as well as the following contributions to the heat flux density \dot{q} :

- Convective heat transfer \dot{q}_c ;
- Heat conduction \dot{q}_{cond} ;
- Absorbed radiant heat flux \dot{q}_r .

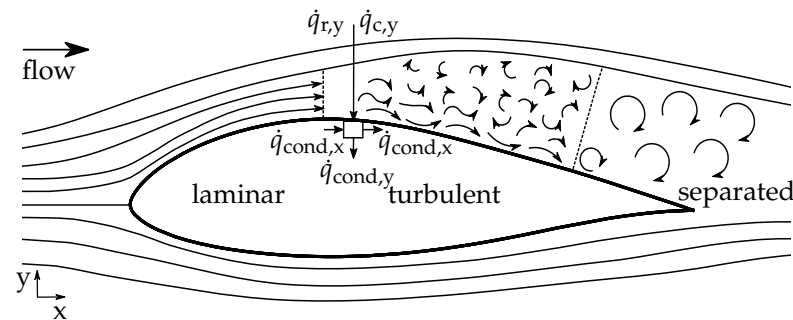


Figure 1. Schematic illustration of the different boundary layer flow regions on the suction side of an airfoil with trailing edge turbulent flow separation. A differential volume element with heat input and output normal to the surface by absorbed radiant heat flux $\dot{q}_{r,y}$, convective heat transfer $\dot{q}_{c,y}$ and heat conduction $\dot{q}_{\text{cond},y}$ are also shown. In the direction of flow, the lateral heat conduction $\dot{q}_{\text{cond},x}$.

For incompressible flows, the convective heat transfer \dot{q}_c depends on the flow-dependent heat transfer coefficient α as well as the temperature difference between the fluid temperature T_{fl} and the surface temperature T_s , and can be calculated by

$$\dot{q}_c = \alpha \cdot (T_s - T_{fl}). \tag{2}$$

Since the intensity of the heat transfer depends on the fluid–surface interaction, the heat transfer coefficient α contains information about the amount and the dynamic of the convective heat transfer for each flow region [25]. Thus, according to Equation (2), different flow conditions lead to different surface temperatures.

In contrast, heat conduction \dot{q}_{cond} , non-isotropic absorbed solar radiation \dot{q}_r and local changes in shape and material M lead to flow-independent spatial temperature gradients. In addition, the dynamic behaviour of the radiation intensity and the temperature of the incoming flow, as well as the initial surface temperature T_0 , influence the distribution and dynamics of the measured surface temperature field. Due to these cross-sensitivities, the different flow regions are not always visible, which means that the thermal contrast between the different flow regions is decreased. Regardless of these influences, the classical concept of thermographic flow visualisation is the evaluation of surface temperature fields as a function of the heat transfer coefficient α as the input signal—see Figure 2a. The new approach aims to use the thermal response of the surface temperature to dynamic changes in the flow temperature or the radiation intensity, respectively—see Figure 2b. As a result, the flow-dependent heat transfer coefficient α is considered as a parameter that determines the thermal response of the surface. The visualisation of different flow regions (and, in particular, stall condition) has a higher contrast and interpretability, because the influence of the convective heat transfer is considered after reducing the influence of the heat input variations so that the former cross-sensitivity is reduced.

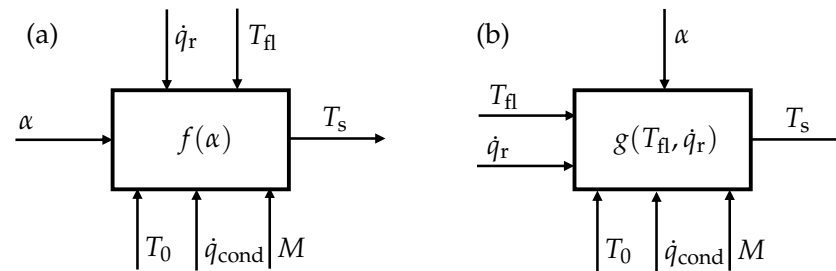


Figure 2. Model function of the surface temperature with input and output quantities and cross-sensitivities, (a): Flow-dependent heat transfer coefficient α as input quantity, (b): Analysis of the response behaviour for changing heat inputs, the flow properties in α are considered as a parameter of the system's input–output relation (cross-sensitivity).

Concerning field measurement conditions on operating wind turbines, the external heat input can have the form of oscillating or transient signals. Oscillating input signals result, e.g., from temporal fluctuations in the temperature of the incoming flow. In contrast, transient changes in radiation intensity and the fluid temperature over the airfoil can induce transient external heat inputs. Therefore, two signal processing approaches are proposed to realise a higher contrast and interpretability of different flow regions by means of a differential evaluation of the surface temperature response to oscillating and transient input signals.

2.1. Thermodynamic Response around an Operating Point

The signal processing approach around an operating point considers the surface temperature response to temporal oscillations in the temperature of the incoming flow. The aim is to identify boundary layer flow regions on the processed thermographic images by means of unambiguous relations between the features of the evaluated surface temperature oscillations and the flow-dependent heat transfer coefficient. Therefore, the surface temperature response behaviour to oscillating input signals is analysed.

Small-scale oscillations in the input signal around an operating point induces thermodynamic oscillations in the output signal. Considering small-scale oscillations around an operating point, the system's input–output relation corresponds to that of a linear time-invariant system. For this reason the input–output relation indicated in Figure 2b is describable with a transfer function and can be evaluated with the powerful methods of linear system theory.

One method for the evaluation of linear systems with harmonic input signals is the analysis of amplitude and phase information for selected frequency components of the output signal. With increasing heat transfer coefficients α , the intensity of the convective heat transport increases and the system's input–output relation has a reduced amplitude attenuation and phase shift [25]. As a result, the amplitude and phase information depends on the heat-transfer coefficient, and thus enables distinguishing between different boundary layer flow regions. Furthermore, the harmonic signal processing approach around an operating point provides two desirable features. First, assuming a negligible dependence of the heat transfer coefficient and the material properties on the surface temperature within the measurement range, the operating point has, on first approximation, no influence of the linear system behaviour around the operating point. Therefore, the amplitudes are independent of the initial temperature field T_0 . Second, due to the harmonic behaviour of the output signal, the influence of the heat conduction is reduced. Thus, spatial differences in amplitude and phase information can only result from different flow properties, i.e., from different heat-transfer coefficients α , or material inhomogeneities M .

Note that the amplitude and phase information depends on the amplitude and the frequency of the available harmonic components in the input signal. In particular, the amplitude response signal and, thus, also the signal-to-noise ratio decreases for increasing frequencies, due to the thermal inertia of the surface [25]. For this reason, the proposed

signal processing approach around an operating point is limited to low-frequency heat input oscillations.

2.2. Transient Thermodynamic Response

In the case of transient input signals, the output signal is also in a transient form and the temporal gradient of the surface temperature field is used to distinguish between different boundary-layer flow regions.

The temperature field of the entire measured object can be described analytically by coupling energy balances and kinetics of heat conduction. For measuring objects with constant thermal conductivity λ , the temperature field T depends on the location, the time t as well as the material properties summarised in the thermal conductivity coefficient a and can be calculated by solving the heat equation [25]

$$\frac{\partial T}{\partial t} = a \nabla^2 T. \quad (3)$$

Thus, the general solution of this differential equation depends on the initial temperature distribution as well as the shape and material parameters denoted as cross-sensitivities T_0 and M , respectively. In addition, the following boundary condition applies to the surface

$$-\lambda \cdot \left(\frac{\partial T}{\partial n} \right)_s = \alpha \cdot (T_s - T_{fl}) + \dot{q}_r, \quad (4)$$

where $\partial/\partial n$ means a normal differentiation on the surface. As a result, the surface temperature response to a transient step-like input signal converges over the time to a steady state temperature. The transient signal processing approach is thus to evaluate the temporal gradient of the surface temperature response. Since transient heat inputs cause enhanced temperature differences between the surface and the fluid temperature, the flow-dependent convective heat flow is the dominant mechanism for the local response behaviour. As a result, the evaluation of temporal temperature gradients leads to a high thermal contrast between the different flow regions. Since the temporal gradient of the surface temperature decreases over time, the measurement will take place at the beginning of the transient input signal.

2.3. Criteria for Flow Region Identification and Distinguishability

Independent of the signal processing approach, the flow regions can only be identified by comparing the processed thermographic images with the flow-dependant heat transfer coefficient α . Therefore, the first criteria for the evaluation of the proposed signal-processing approaches is the unambiguous *identification* of flow regions by means of flow-dependent heat transfer features on the processed thermographic images. As a result, an estimation of the local heat transfer coefficient is needed.

In order to estimate the qualitative behaviour of the local heat transfer coefficient, the well-known heat transfer behaviour on a smooth circular cylinder with supercritical cross-flow is used as a reference. The following features of the heat transfer coefficient are available to realize an identification of different flow regions [23,26]:

- Laminar flow region: α decreases as a result of the decreasing wall shear stress.
- Laminar-turbulent flow transition: α increases sharply as a result of the increased turbulent mixing in the turbulent flow region.
- Turbulent flow region: α decreases as a result of the decreasing wall shear stress.
- Separated flow region: α increases, due to the increased transverse exchange of fluid in the turbulent separated flow region induced by grown vortices. In contrast to attached flow regions, large-scale vortices are the dominant mechanism for convective heat transfer in separated flow regions.

The result of the harmonic signal processing approach around an operating point corresponds directly to the presented features of the heat transfer coefficient and enables a subsequent identification of flow regions. In contrast, the gradient-based evaluation for transient input signals requires a consideration of the initial surface temperature T_0 in order to be able to detect flow-dependent features and identify the different flow regions. Note that the mentioned qualitative local heat transfer features are approximately expected for the flow velocities and rotor blade profiles at wind turbines, due to the underlying boundary layer mechanisms. However, a precise estimation of the local heat transfer behaviour requires a more detailed consideration of the geometry and surface properties of the measurement object as well as the incoming flow conditions.

As second evaluation criteria, the contrast-to-noise ratio (CNR) is calculated, which is a common approach in order to quantify the *distinguishability* between a pair of flow regions. The CNR between the flow regions a, b is calculated by

$$\text{CNR} = \frac{|\bar{C}_a - \bar{C}_b|}{\sqrt{\left(\frac{1}{N_a} \sum_{i=1}^{N_a} s_{a,i}\right)^2 + \left(\frac{1}{N_b} \sum_{j=1}^{N_b} s_{b,j}\right)^2}}. \quad (5)$$

The spatial image dimension is $M \times N$ pixel, where M represents the model span and N the chord length. \bar{C}_a, \bar{C}_b are the spatial mean of the pixels within a flow region. While $s_{a,i}, s_{b,j}$ describes the corresponding standard deviation transverse to the flow direction. The standard deviation is calculated transverse to the flow direction in order to reduce the influence of gradients on the processed images along the flow direction.

3. Experimental Setup

3.1. Wind Tunnel Setup and Experimental Procedures

In order to investigate the potential of the presented signal-processing approaches, measurements at Deutsche WindGuard's aeroacoustically optimized wind tunnel (DWAA) in Bremerhaven, Germany are conducted. The Göttinger-type wind tunnel operates with a closed test section with turbulence intensities of less than 0.3% at wind speeds of up to 100 m s^{-1} . The test section has a dimension of $1.25 \text{ m} \times 2.7 \text{ m} \times 5 \text{ m}$. The aerodynamic models, with a maximal chord length of up to 0.9 m, are vertically mounted between two turntables at the ceiling and the floor of the test section, which allows for adjusting different angles of attack. The thermographic camera is positioned on the side of the wind tunnel test section, facing the measurement object through a window made of calcium fluoride. Figure 3 illustrates the experimental setup. Note that the friction in the wind tunnel due to operation is the only external heat source and leads to an increasing fluid temperature during the measurements. In addition to the large-scale fluid temperature gradient, there are small-scale fluid temperature oscillations that are probably a result of variations in the fan power. Due to the inertia of the power control, the oscillations are mainly in a low-frequency range from 0 to 0.2 Hz.

For the presented measurements, a wind turbine airfoil of type DU96W180 is selected. The wind tunnel model has a chord length of 0.6 m, height of 1.25 m and is made out of carbon reinforced plastic with a polyurethane topcoat which is typical for rotor blades of wind turbines [8]. Figure 4 shows the mounted airfoil profile inside the wind tunnel measuring section. Note that the profile does not have a homogeneous surface, since a mylar band covers a flap-gap at the 0.82 normalised chord position. Piezo pressure sensors are attached to the upper and lower side of the airfoil as a reference measuring system for the detection and localisation of laminar-turbulent transition and flow separation. The 92 pressure sensors along the chord length in flow direction are connected to pressure tabs in the surface of the airfoil and provide a sampling rate of 10 Hz. The tabs are located not behind each other but with a spanwise offset, in order to avoid impacts on the boundary layer flow and subsequently the downstream pressure measurements.

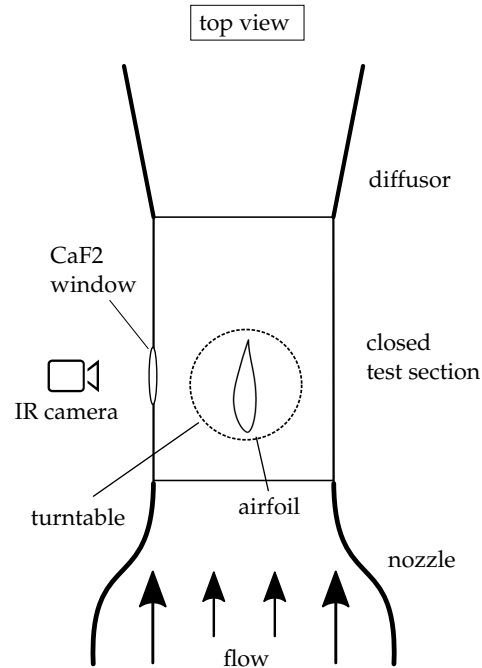


Figure 3. Schematic overview of the measurement setup in the closed test section of the Deutsche WindGuard's aeroacoustic wind tunnel in Bremerhaven, Germany, adapted from [20].

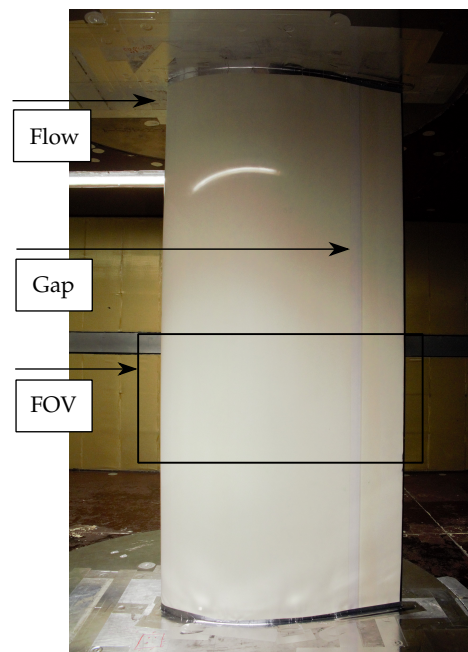


Figure 4. Suction side of the mounted DU96W180 profile in the test section with marked field of view (FOV) of the thermographic camera.

In order to characterise the proposed signal processing approaches, the experiments are designed for two free-field similar measurement conditions. Firstly, measurements with a low thermal contrast on a measurement object in a near thermodynamic steady state are conducted. Here, the focus is on the harmonic evaluation of the surface temperature response to small-scale oscillations of the input signal (*thermodynamic response around an operating point*). Secondly, the flow velocity is increased in order to increase the heating rate of the wind tunnel. Consequently, the fluid temperature is considered as a transient input signal and the gradient-based signal processing approach is characterised (*transient thermodynamic response*). Note that the harmonic signal processing approach around an

operating point evaluates the surface temperature oscillations which occur independent of the large-scale behaviour of the surface temperature. Therefore, the harmonic approach is applicable for both measurement conditions, while the gradient-based approach is limited to transient input signals.

The adjusted test parameters are the incoming flow velocity, the compensation time before starting the experiments and the angle of attack of the measurement object. In order to achieve a near thermodynamic steady state the mean flow velocity is set to 49 m s^{-1} and the measurement starts after a compensation time of 10 min. The measurement with a transient input signal is conducted for a flow velocity of 74 m s^{-1} , the measurement starts directly after the wind tunnel start-up phase. The flow velocities result in the Reynolds numbers $Re = 2 \cdot 10^6$ and $Re = 3 \cdot 10^6$, respectively, and emulate realistic flow velocities for rotor blades of wind turbines [27]. With respect to the defined flow velocities, the angle of attack is set to $AoA = 14^\circ$ for both experiments, which leads to the existence of laminar, turbulent and separated boundary layer flow regions. Note that the maximum flow velocity of 74 m s^{-1} leads to a Mach number of about 0.22. Considering the chosen angle of attack, as well as the resulting surface pressure gradient, weak compressibility effects of the flow are possible, but have only a negligible influence on the evaluated boundary layer properties.

Figure 5 shows the averaged profile temperature of the surface over the measurement time for both measurement conditions. Aside from the large scale behaviour depending on the flow velocity, small-scale oscillations are visible.

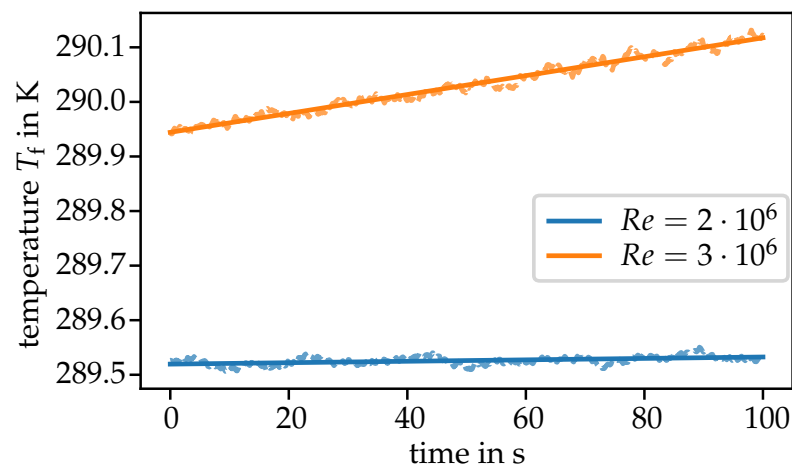


Figure 5. Linear regression of the averaged profile surface temperature over the measurement period for $Re = 2 \cdot 10^6$ and $Re = 3 \cdot 10^6$. The small-scale oscillations of the surface temperature are visible by dashed lines.

For $Re = 2 \cdot 10^6$, the wind tunnel heating rate is about 0.01 K min^{-1} , which leads to a low thermal contrast and short compensation time to achieve the desired near-thermodynamic steady state of the measurement object. For a $Re = 3 \cdot 10^6$, a transient input signal is realised by a fluid temperature ramp with a heating rate of about 0.1 K min^{-1} .

3.2. Thermographic Image Acquisition

The thermographic camera, type imageIR8300, from the manufacturer InfraTec is used. The camera is sensitive for wavelengths between $2\text{--}5.7 \mu\text{m}$, works with an actively cooled InSb focal plane array and a global shutter, has a pixel size of $15 \mu\text{m}$ and provides a dynamic range of 14 bit. The noise equivalent temperature difference (NETD) is less than 25 mK at 30°C . Furthermore, the curved object geometry causes a non-uniform temperature distribution as a consequence of the angle-dependent emissivity. The thermographic camera is equipped with a 12 mm wide-angle lens. At the viewing distance of 1.52 m , the instantaneous field of view has a spatial resolution of 1.9 mm on the object surface represented by one pixel and 312 measurement points over the chord length.

As a result of the surface curvature of the airfoil and the camera lens, the image is distorted both in perspective and optically. With the aim to reduce the distortion effects and to reach straight edges of the measuring object, a correction of optical distortion is conducted. For the presented measurements, with measurement times of 100 s, the camera integration time is set to 1600 μ s. The sampling rate is 300 Hz, which is the maximum value for the presented camera setup.

3.3. Image Processing

The evaluation of the dynamic surface temperature response of the resulting image series is based on the temporal evaluation of single pixels with image series consisting of J images. The spatial dimension of each image is $M \times N = 151 \times 386$ pixels, and for the region of interest, i.e., without background, 151×312 pixels. According to the different signal processing approaches, two different evaluation methods are used.

The evaluation of the surface temperature response to transient input signals is based on time-averaged temporal temperature gradients $d\bar{T}_{s,mn}$, which are calculated by

$$\bar{dT}_{s,mn} = \frac{1}{J-1} \sum_{j=0}^{J-2} (T_{s,mn}(j+1) - T_{s,mn}(j)). \quad (6)$$

where, j denotes the time step and m, n pixel row and pixel column, respectively.

In order to analyse the surface temperature response around predefined operating points, firstly the temporal temperature gradients are deducted from the measured data using a linear regression function. As a result, evaluation around an operating point only takes place for the oscillating part of the input signal and is independent of the input signals' large-scale behaviour. Subsequently, the surface temperature response is evaluated by harmonic amplitudes. For this reason, a pixelwise discrete Fourier transformation is performed in order to calculate the Fourier coefficients $P_{mn}(k)$ for each frequency component k , according to

$$P_{mn}(k) = \frac{1}{J} \sum_{j=0}^{J-1} \exp\left(-2\pi i \frac{jk}{J}\right) T_{s,mn}(j), \quad k = 0, \dots, J-1. \quad (7)$$

With the aim to evaluate the surface temperature response to fluid temperature oscillations, the Fourier coefficients are filtered for the frequency range of the fluid temperature oscillation. Therefore, the frequency range is limited to 0–0.2 Hz in order to achieve the maximum signal-to-noise ratio. Finally, an averaging over the K filtered Fourier coefficients is conducted, in order to attain the mean amplitude

$$\bar{P}_{mn} = \frac{1}{K} \sum_{k=1}^K P_{mn}(k), \quad (8)$$

as the evaluation quantity of the harmonic signal processing approach around an operating point.

In addition, the classical approach of calculating time-averaged temporal surface temperatures $\bar{T}_{s,mn}$ is used as reference method. The temporal mean surface temperatures are calculated by

$$\bar{T}_{s,mn} = \frac{1}{J} \sum_{j=0}^{J-1} T_{s,mn}(j). \quad (9)$$

The aim is to evaluate improvements in the proposed dynamic signal processing approaches compared to the classical approach regarding identifiability and distinguishability of flow regions. Comparison criteria are the identifiability of flow regions using flow-dependent features and the calculated contrast-to-noise ratio between different flow regions according to Equation (5).

4. Results

4.1. Near Thermodynamic Steady State Condition

In order to compare the different signal processing approaches for a measurement object in a near thermodynamic steady state, the location of the turbulent boundary separation for $Re = 2 \cdot 10^6$ is identified at first. Surface pressure measurements on the suction side of the airfoil serve as a reference, and the dimensionless pressure coefficient c_p is calculated by:

$$c_p = \frac{p - p_\infty}{0.5\rho_\infty U_\infty^2}, \quad (10)$$

where p denotes the static pressure on the airfoil surface, p_∞ and U_∞ are the static pressure and the flow velocity of the undisturbed incoming flow, respectively, and ρ_∞ is the fluid density.

Figure 6 shows the experimental values of the dimensionless pressure coefficient c_p , including the 99% confidence interval as error bars over the normalized chord position x/c for different angles of attack AoA , where c is the chord length. In addition to the pressure distributions of the presented experiment with $AoA = 14^\circ$, the pressure distributions for experiments without flow separation, i.e., with lower angles of attack of 2° , 6° and 10° , are plotted for comparison. For the presented experiment, the turbulent boundary layer separation is detected at $x/c = 0.46$ due to the constant values of the dimensionless pressure coefficient induced by the constant static pressure in separated flow regions [2,28]. For comparison, at lower angles of attack without flow separation, positive pressure gradients are visible in the region from $x/c = 0.46$ to $x/c = 1$.

In order to estimate the position of the laminar-turbulent flow transition for the presented experiment with $AoA = 14^\circ$, the thermographic detectable movement of the transition position for the measurements with the angle of attack of 2° , 6° and 10° is used as a reference. As shown in Figure 7, the transition position moves from $x/c = 0.55$ for $AoA = 2^\circ$ to $x/c = 0.15$ for $AoA = 10^\circ$. As a result, the position of the laminar-turbulent transition is expected to be near the leading edge for $AoA = 14^\circ$.

The subsequent respective comparison of the thermographic flow visualization with the different signal processing concepts is performed on the basis of the evaluation criteria introduced in Section 2.3:

- Identifiability of flow regions on the basis of characteristic flow-dependent features;
- Distinguishability between flow regions using the contrast-to-noise ratio.

For this purpose, the image processing results of the mean temperature (classical approach) as well as the novel gradient-based and the around-an-operating-point signal processing approach are shown in Figure 8 for the flow condition $Re = 2 \cdot 10^6$. Figure 8a–c show the output images in order to analyse the distinguishability between the different flow regions. The averaged profiles over the normalized chord position are shown in Figure 8d–f with the aim of identifying flow-dependent features.

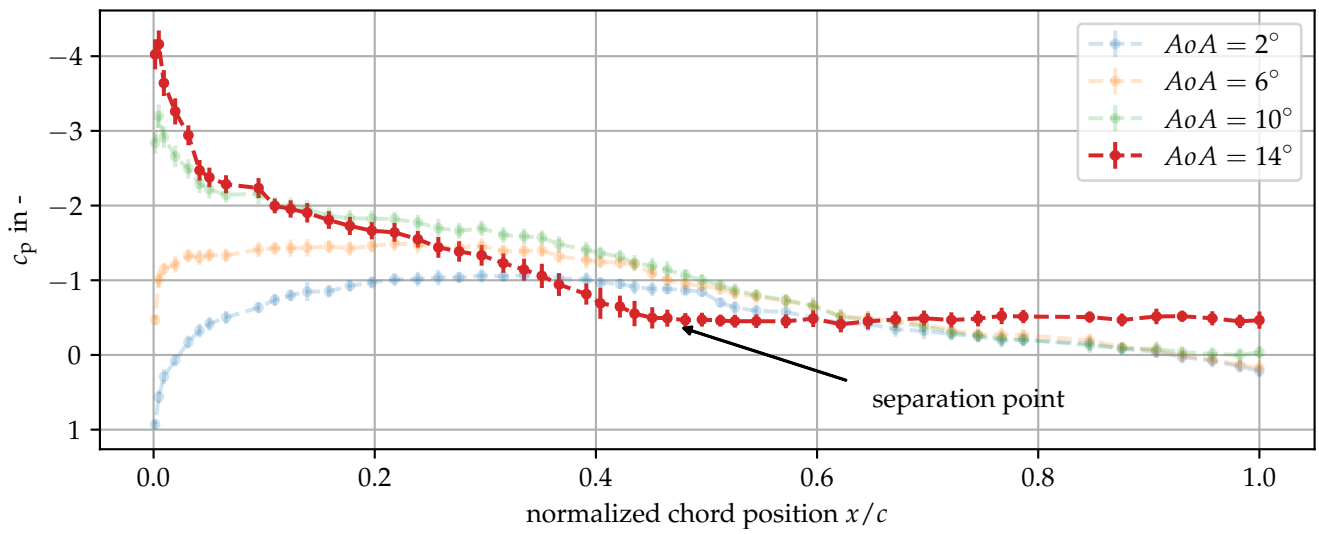


Figure 6. Distribution of experimental determined dimensionless pressure coefficients c_p on the suction side of the airfoil of type DU96W180 for a Reynolds numbers of $Re = 2 \cdot 10^6$.

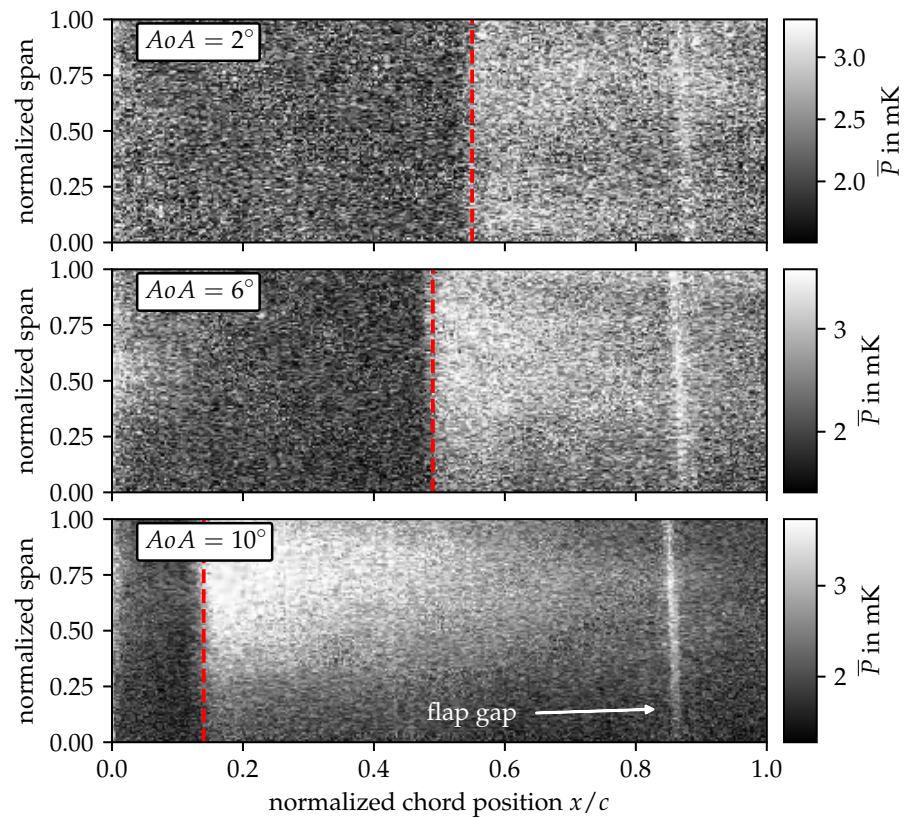


Figure 7. Comparison of the laminar-turbulent flow transition position (dashed lines) for variable angle of attack by means of the evaluation of thermographic image series with the harmonic signal processing approach. Experimental parameters: variable angle of attack, $Re = 2 \cdot 10^6$.

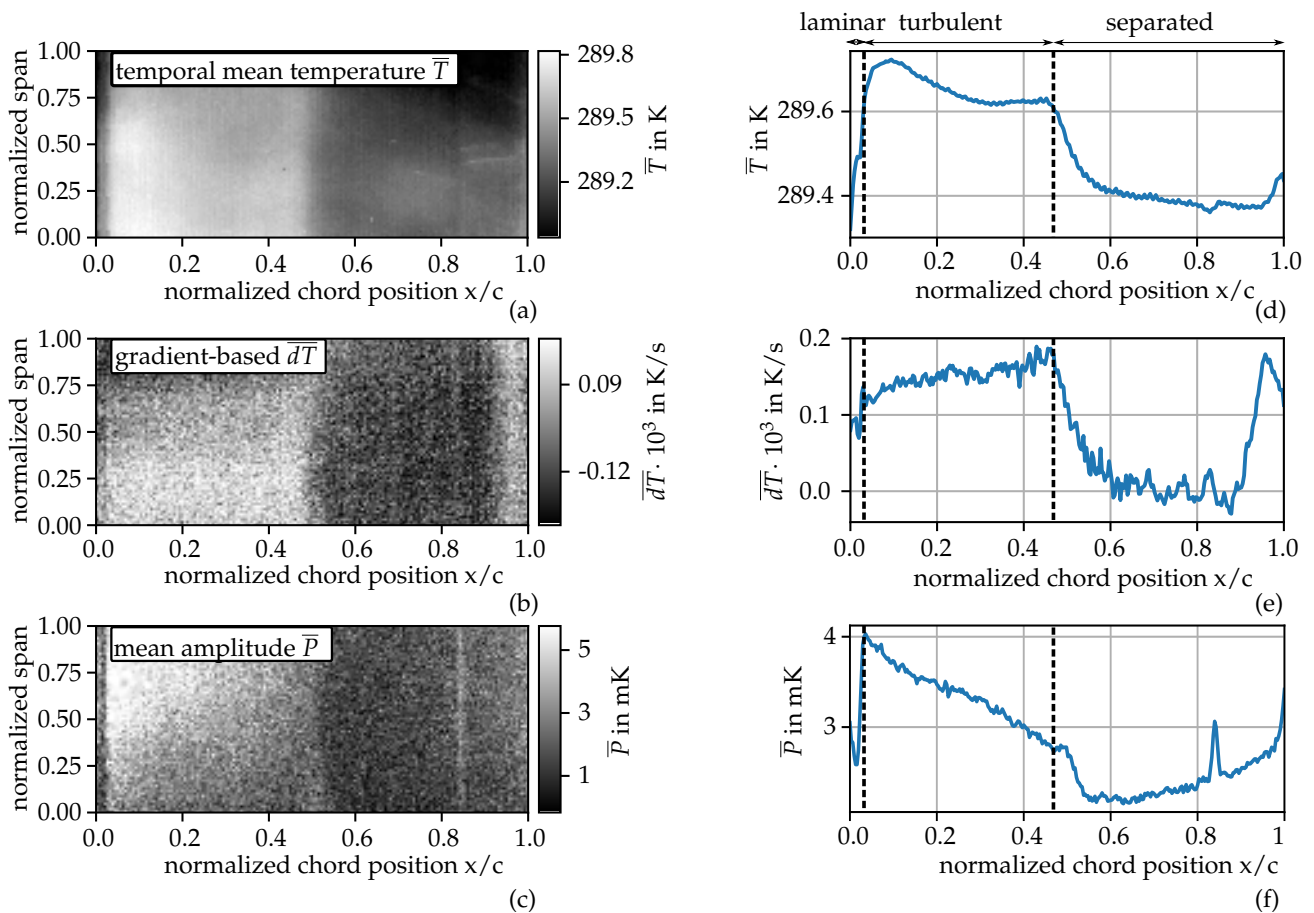


Figure 8. Comparison of the evaluation of thermographic image series by the mean temperature (a,d), gradient-based (b,e) and the harmonic signal processing approach (c,f) for a measuring object with near thermodynamic steady state behaviour. Left side (a–c): processed thermographic images, right side (d–f): averaged profiles over the chord position. Experimental parameters: $Re = 2 \cdot 10^6$, $AoA = 14^\circ$.

4.1.1. Identifiability

Considering the evaluation criteria of the identifiability of flow regions on the basis of flow-dependent features, the mean temperature signal-processing approach as a classical concept is analysed at first. The mean temperature course over the normalized chord position in Figure 8d shows the estimated signal behaviour for the transition regions and enables distinguishing different flow regions. However, the temperature course within the single flow regions is mainly influenced by lateral heat conduction, see Section 2.1. In consequence, an unambiguous feature-based identification of flow regions is impossible. In particular, the identifiability of flow separation is reduced, as the temperature gradient along the chord position is similar in turbulent and separated flow regions.

Since the measurement object is in a near thermodynamic steady state, the gradient-based evaluation in Figure 8e shows small absolute values of the temporal gradients. Within the laminar and the turbulent flow region, the convective heat input \dot{q}_c is higher than the heat emission by radiation \dot{q}_r , which explains the positive gradient. For the normalized chord position (0.6–0.85) within the separated flow region, the surface of the measurement object is already approximately in a thermodynamic steady state. The increasing gradient and the local maximum at the normalized chord position (0.85–1) are explained by the increasing heat transfer coefficient, as well as a heat input by heat conduction from the pressure side of the airfoil. As a result, the different flow regions are only identifiable under a complex consideration of the cross-sensitivities.

In contrast, the result of the harmonic signal processing approach around an operating point reflects the qualitative estimations of the heat transfer coefficient and enables the localisation of the flow regions, as follows:

- Laminar boundary layer flow: $0 \leq x/c \leq 0.02$;
- Laminar-turbulent transition: $0.02 < x/c \leq 0.04$ (dashed lines);
- Turbulent-boundary layer flow: $0.04 < x/c \leq 0.46$;
- Turbulent separation point: about 0.46 (dashed lines);
- Turbulent separated boundary layer flow: $0.46 < x/c \leq 1$.

The evaluation of the amplitude course in Figure 8f shows a continuously decreasing amplitude over the normalized chord position as a result of a decreasing wall shear stress within the attached flow regions. In contrast, the evaluated amplitude increases within the separated flow region due to the increasing heat transfer coefficient. Furthermore, sharp transitions are detectable as a result of the reduced influence of lateral heat conduction. In addition, the capability to detect surface modifications, which is a beneficial property of the harmonic signal processing approach around an operating point, is shown at the 0.82 normalized chord position with a clearly visible local amplitude maximum. Thus, the signal processing approach around an operating point provides a high degree of interpretability and enables an unambiguous feature-based identification of flow regions. In particular, the aim of an improved identifiability of flow separation is realised.

4.1.2. Distinguishability

In order to compare the measurement approaches in terms of the quantitative distinguishability of the different flow regions, the CNR between the flow regions is presented in Table 1. The highest CNR between laminar-turbulent and turbulent-separated flow regions is achieved with the classical mean temperature approach. As expected, the gradient-based signal processing approach provides less distinguishability of the flow regions for a measurement object at near thermodynamic steady state. However, a distinction between the turbulent and the separated flow region is possible. For the presented measurement, the signal processing approach around an operating point provides a reduced CNR of about -54% and -35% between laminar-turbulent and turbulent-separated flow regions, respectively, compared to the classical mean temperature approach. One reason for the reduced contrast is the small-signal behaviour of the surface temperature oscillation with a magnitude of about 5 mK which is smaller than the NETD of the camera for a single image. Accordingly, the harmonic signal processing approach around an operating point takes place for signals with a low signal-to-noise ratio, which explains the reduced distinguishability between the flow regions.

Table 1. Comparison of the contrast-to-noise ratio for the proposed signal processing approaches for a measuring object at near thermodynamic steady state: mean temperature $\text{CNR}_{\bar{T}}$, gradient-based $\text{CNR}_{\bar{dT}}$, harmonic signal processing approach $\text{CNR}_{\bar{p}}$.

Pair of Flow Regions	$\text{CNR}_{\bar{T}}$	$\text{CNR}_{\bar{dT}}$	$\text{CNR}_{\bar{p}}$
laminar–turbulent	2.1	0.46	0.97
turbulent–separated	2.46	1.12	1.6

In consequence, the proposed signal processing approaches do not enhance the distinguishability of the flow regions for measuring objects at a near thermodynamic steady state under the studied flow conditions. However, an improvement in the distinguishability between flow regions using the harmonic signal processing approach around an operating point can occur for measurement conditions with a further reduced convective heat input.

4.2. Transient Thermodynamic State Condition

In order to characterise the proposed signal processing approaches for a transient input signal, the image processing result for the measurement with $Re = 3 \cdot 10^6$ is shown

in Figure 9. In detail, Figure 9a–c show the resulting images for each signal processing approach, while Figure 9d–f show the averaged profiles over the chord position and the location of the different flow regions. The location of the boundaries was validated again by surface pressure measurements as a reference.

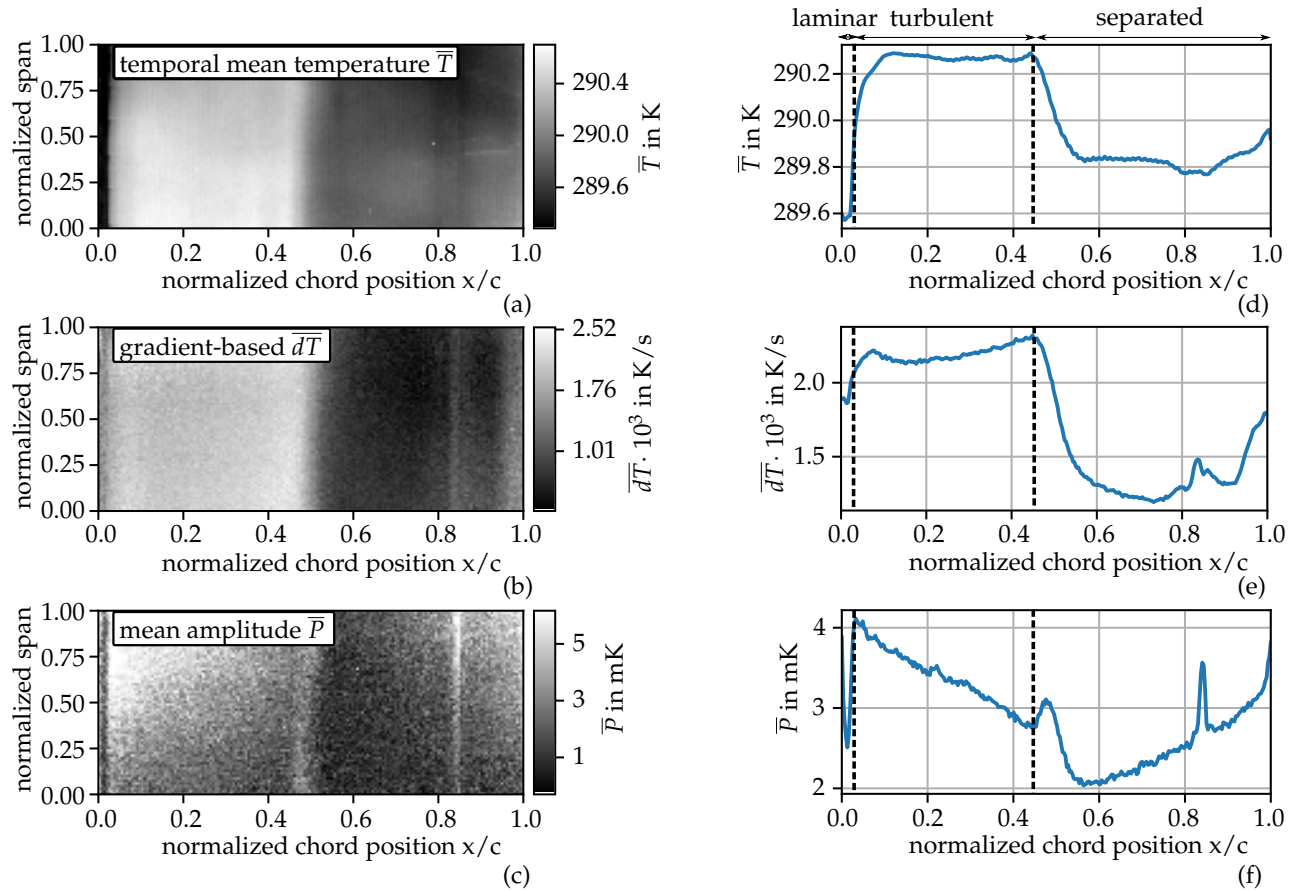


Figure 9. Comparison of the evaluation of thermographic image series by the mean temperature (a,d), gradient-based (b,e) and the harmonic signal processing approach (c,f) for a transient input signal. Left side (a–c): processed thermographic images; right side (d–f): averaged profiles over the normalized chord position. Experimental parameters: $Re = 3 \cdot 10^6$, $AoA = 14^\circ$.

4.2.1. Identifiability

Comparing the identifiability of the flow regions for the classical mean temperature signal processing approach in Figure 9d, with the result for a measurement object near a thermodynamic steady state in Figure 8d, the influence of heat conduction on the temperature course is reduced as a result of the enhanced convective heat input for the measurement with $Re = 3 \cdot 10^6$. However, characteristic features within the single flow regions are not detectable, despite the enhanced convective heat input.

Evaluating the surface temperature response to a transient input signal with the gradient-based signal-processing approach in terms of identifiability of flow regions, Figure 9e shows an improved result compared to the mean temperature signal processing approach. As a result of the dominant influence of the flow-dependent convective heat transfer for the local response behaviour, flow-dependent features are partly within the single flow regions visible and even the surface modification at 0.82 normalized chord position is detectable. For a complete interpretation of the gradient course over the normalized chord position, however, a separate consideration of the influences of the surface temperature distribution and the heat conduction is required. For example, the parabolic shape of the gradient in the turbulent and the separated flow region contradicts the esti-

mation of a continuous signal decrease and increase, respectively, over the chord position, see Section 2.3. As a result, the gradient-based signal processing approach is also for a transient input signal, but is not suitable for an unambiguous feature-based identification of flow regions.

In contrast, the harmonic signal processing approach around an operating point enables a complete interpretation of the evaluated amplitude course over the normalized chord position in Figure 9f on the basis of the estimated flow-dependent features. In particular, the separation point is clearly identifiable by means of a subsequent local amplitude maximum followed by a global amplitude minimum at approximate 0.45 and 0.55 normalised chord positions, respectively. As a result, the harmonic signal processing approach around an operating point improves the identifiability of the flow regions, independent of the large scale behaviour of the surface temperature.

4.2.2. Distinguishability

For the comparison of the signal processing approaches in terms of distinguishability between the different flow regions for a transient input signal, the respective CNR is calculated and summarized in Table 2.

Table 2. Comparison of the contrast to noise ratio for the proposed signal processing approaches for a transient input signal: mean temperature \bar{T} , gradient-based \overline{dT} , harmonic signal processing approach \bar{P} . Additionally, a comparison of the respective CNR change for the different measurement conditions.

Approach	Pair of Flow Regions	CNR	Change
\bar{T}	laminar–turbulent	6.88	227.62%
	turbulent–separated	3.39	37.8%
\overline{dT}	laminar–turbulent	2.39	419.57%
	turbulent–separated	6.88	514.29%
\bar{P}	laminar–turbulent	0.67	−30.93%
	turbulent–separated	1.33	−16.88%

Firstly, the enhanced convective heat input for the measurement with $Re = 3 \cdot 10^6$ causes an increasing CNR of the mean temperature and the gradient-based signal processing approach. In contrast, the harmonic signal processing approach around an operating point provides a reduced CNR, compared to the near thermodynamic steady state condition at $Re = 2 \cdot 10^6$, as a result of the enhanced heat transfer coefficients in the laminar and separated flow region. Therefore, the harmonic signal processing approach around an operating point is for measurements with a high convective heat input not suitable to increase the distinguishability between flow regions.

Regarding the distinguishability of different flow regions, the gradient-based signal processing approach provides the highest CNR between turbulent-separated flow regions. Compared to the mean temperature approach, a significant improvement in the CNR of about 103 % is achieved. For the distinction between laminar and turbulent flow regions, the mean temperature signal processing approach provides a higher CNR than the gradient-based approach as a result of the relationship between the convective heat input and the surface temperature distribution. According to Equation (2), the convective heat input depends on the heat transfer coefficient α as well as the temperature difference between the fluid temperature T_f and the surface temperature T_s . In the presented case of a low CNR between laminar-turbulent flow regions when using the gradient-based signal processing approach, flow-dependent differences in convective heat input are reduced due to the high temperature difference between the considered flow regions. However, the aim to enhance the contrast for stall detection is realised with the gradient-based signal processing approach.

5. Conclusions and Outlook

Two signal processing approaches were proposed to achieve an enhanced detectability of flow separation using thermographic image series: a harmonic analysis of the small signal behaviour and a gradient-based evaluation of the large signal behaviour. By rigorously deriving both signal-processing approaches from an analysis of the signal measurement chain and evaluating the surface temperature response according to the dynamic behaviour of the incoming flow temperature, a higher degree of interpretability and distinguishability between the different flow regions is obtained.

The amplitude information of the proposed harmonic signal processing approach around an operating point is shown to contain only the surface temperature response to the oscillating parts of the incoming flow temperature. Subsequently, the amplitude information provides a direct correlation with the flow-dependent mean value of the heat transfer coefficient. As a result, the harmonic signal-processing approach around an operating point enables an unambiguous identification of flow regions on the basis of flow-dependent features. In particular, the identifiability of flow separation is increased by a global minimum in the amplitude curve over the chord position near the separation point. In addition, the harmonic signal processing approach around an operating point leads to an increased spatial resolution for surface modifications. However, the contrast between the flow regions is significantly decreased compared to the classical signal processing approach, i.e., when evaluating the mean value of the surface temperature. Therefore, the harmonic signal processing approach around an operating point can be considered as a reference method for the identification of flow regions and is especially useful for measurement objects at near thermodynamic steady state, i.e., in applications with a low thermal contrast between the different flow regions.

The second proposed signal processing approach, which evaluates the surface temperature response to a transient input signal (from the incoming flow temperature) on the basis of the temporal temperature gradient, provides an improved contrast for the thermographic detection of flow separation. However, the applicability of the approach is limited to measurement objects with a transient thermodynamic behaviour. As a result, the gradient approach provides an improved distinguishability and location of flow transitions on the basis of the CNR in case of a transient input signal. Instead, the harmonic approach enables an unambiguous distinction between attached and separated flow regions. Therefore, both proposed signal processing approaches are a supplement to the established evaluation of temporal mean temperatures.

In the present work, the suitability of the novel signal processing approaches for the detection of flow separation in wind tunnel experiments was proven. Further research will focus on the method transfer to free-field measurements. The next aim is to detect flow separation on rotor blades of wind turbines in operation.

Author Contributions: Conceptualization, F.O., M.S. and A.F.; methodology, F.O. and A.F.; software, F.O.; validation, F.O., D.G. and A.F.; investigation, F.O., D.G., J.S., N.B. and A.F.; resources, F.O., J.S., N.B. and A.F.; writing—original draft preparation, F.O., M.S. and A.F.; writing—review and editing, F.O., J.S., N.B., M.S. and A.F.; visualization, F.O. and A.F.; supervision, M.S. and A.F.; project administration, F.O., M.S. and A.F.; funding acquisition, M.S. and A.F. All authors have read and agreed to the published version of the manuscript.

Funding: This research was funded by the Deutsche Forschungsgemeinschaft (DFG project number FI 1989/5-1).

Institutional Review Board Statement: Not applicable.

Informed Consent Statement: Not applicable.

Data Availability Statement: Not applicable.

Acknowledgments: The authors gratefully acknowledge the loan of the rotor blade model by the TU Delft.

Conflicts of Interest: The authors declare no conflict of interest.

References

1. Martinez Suarez, J.; Flaszynski, P.; Doerffer, P. Application of rod vortex generators for flow separation reduction on wind turbine rotor. *Wind Energy* **2018**, *21*, 1202–1215. [\[CrossRef\]](#)
2. Schlichting, H.; Gersten, K. *Boundary-Layer Theory*, 9th ed.; Springer: Berlin/Heidelberg, Germany, 2017; [\[CrossRef\]](#)
3. Gad-el Hak, M.; Bushnell, D.M. Separation Control: Review. *J. Fluids Eng.* **1991**, *113*, 5–30. [\[CrossRef\]](#)
4. Pellegrino, A.; Meskell, C. Vortex shedding from a wind turbine blade section at high angles of attack. *J. Wind. Eng. Ind. Aerodyn.* **2013**, *121*, 131–137. [\[CrossRef\]](#)
5. Vey, S.; Lang, H.M.; Nayeri, C.N.; Paschereit, C.O.; Pechlivanoglou, G. Extracting quantitative data from tuft flow visualizations on utility scale wind turbines. *J. Phys. Conf. Ser.* **2014**, *524*, 012011. [\[CrossRef\]](#)
6. Corten, G.P.; Veldkamp, H.F. Insects can halve wind-turbine power. *Nature* **2001**, *412*, 41–42. [\[CrossRef\]](#)
7. Medina, P.; Schreck, S.; Johansen, J.; Fingersh, L. Oil-flow visualization on a SWT-2.3-101 wind turbine. In Proceedings of the 29th AIAA Applied Aerodynamics Conference, Honolulu, HI, USA, 27–30 June 2011; American Institute of Aeronautics and Astronautics: Reston, VA, USA, 2011; p. 06272011. [\[CrossRef\]](#)
8. Dollinger, C.; Balaesque, N.; Sorg, M.; Fischer, A. IR thermographic visualization of flow separation in applications with low thermal contrast. *Infrared Phys. Technol.* **2018**, *88*, 254–264. [\[CrossRef\]](#)
9. Gartenberg, E.; Roberts, A.S. Twenty-five years of aerodynamic research with infrared imaging. *J. Aircr.* **1992**, *29*, 161–171. [\[CrossRef\]](#)
10. Incropera, F.P. *Fundamentals of Heat and Mass Transfer*, 6th ed.; John Wiley: Hoboken, NJ, USA, 2007.
11. Simon, B.; Filius, A.; Tropea, C.; Grundmann, S. IR thermography for dynamic detection of laminar-turbulent transition. *Exp. Fluids* **2016**, *57*, 93. [\[CrossRef\]](#)
12. Gartenberg, E.; Roberts, A.S. Airfoil transition and separation studies using an infrared imaging system. *J. Aircr.* **1991**, *28*, 225–230. [\[CrossRef\]](#)
13. Ricci, R.; Montelpare, S. Analysis of boundary layer separation phenomena by infrared thermography Use of acoustic and/or mechanical devices to avoid or reduce the laminar separation bubble effects. *Quant. InfraRed Thermogr. J.* **2009**, *6*, 101–125. [\[CrossRef\]](#)
14. Ricci, R.; Montelpare, S.; Silvi, E. Study of acoustic disturbances effect on laminar separation bubble by IR thermography. *Exp. Therm. Fluid Sci.* **2007**, *31*, 349–359. [\[CrossRef\]](#)
15. Ricci, R.; Montelpare, S.; Renzi, E. Study of mechanical disturbances effects on the laminar separation bubble by means of infrared thermography. *Int. J. Therm. Sci.* **2011**, *50*, 2091–2103. [\[CrossRef\]](#)
16. Quast, A. Detection of transition by infrared image techniques. *Tech. Soar.* **1987**, *30*, 33–38.
17. de Luca, L.; Carlomagno, G.M.; Buresti, G. Boundary layer diagnostics by means of an infrared scanning radiometer. *Exp. Fluids* **1990**, *9*, 121–128. [\[CrossRef\]](#)
18. Dollinger, C.; Sorg, M.; Balaesque, N.; Fischer, A. Measurement uncertainty of IR thermographic flow visualization measurements for transition detection on wind turbines in operation. *Exp. Therm. Fluid Sci.* **2018**, *97*, 279–289. [\[CrossRef\]](#)
19. Dollinger, C.; Balaesque, N.; Gaudern, N.; Gleichauf, D.; Sorg, M.; Fischer, A. IR thermographic flow visualization for the quantification of boundary layer flow disturbances due to the leading edge condition. *Renew. Energy* **2019**, *138*, 709–721. [\[CrossRef\]](#)
20. Gleichauf, D.; Dollinger, C.; Balaesque, N.; Gardner, A.D.; Sorg, M.; Fischer, A. Thermographic flow visualization by means of non-negative matrix factorization. *Int. J. Heat Fluid Flow* **2020**, *82*, 108528. [\[CrossRef\]](#)
21. Raffel, M.; Merz, C.B.; Schwermer, T.; Richter, K. Differential infrared thermography for boundary layer transition detection on pitching rotor blade models. *Exp. Fluids* **2015**, *56*, 1–13. [\[CrossRef\]](#)
22. Gartenberg, E.; Wright, R.E. Boundary-layer transition detection with infrared imaging emphasizing cryogenic applications. *AIAA J.* **1994**, *32*, 1875–1882. [\[CrossRef\]](#)
23. Gorin, A.V. Turbulent Separated Flows: Near-Wall Behavior and Heat and Mass Transfer. *J. Appl. Fluid Mech.* **2008**, *1*, 71–77.
24. Gardner, A.D.; Wolf, C.C.; Raffel, M. A new method of dynamic and static stall detection using infrared thermography. *Exp. Fluids* **2016**, *57*, 1–13. [\[CrossRef\]](#)
25. *VDI Heat Atlas*, 2nd ed.; VDI-Buch; Springer: Berlin, Germany, 2010; [\[CrossRef\]](#)
26. Achenbach, E. Total and local heat transfer from a smooth circular cylinder in cross-flow at high Reynolds number. *Int. J. Heat Mass Transf.* **1975**, *18*, 1387–1396. [\[CrossRef\]](#)
27. Hau, E. *Wind Turbines*; Springer: Berlin/Heidelberg, Germany, 2013; [\[CrossRef\]](#)
28. Tani, I. Low-speed flows involving bubble separations. *Prog. Aerosp. Sci.* **1964**, *5*, 70–103. [\[CrossRef\]](#)